Shell model Monte Carlo investigation of rare earth nuclei

J. A. White and S. E. Koonin
W. K. Kellogg Radiation Laboratory, 106-38, California Institute of Technology, Pasadena, California 91125

D. J. Dean
Physics Division, Oak Ridge National Laboratory, P.O. Box 2008, Oak Ridge, Tennessee 37831-6373
and Department of Physics and Astronomy, University of Tennessee, Knoxville, Tennessee 37996
(Received 17 December 1998; revised manuscript received 21 October 1999; published 14 February 2000)

We utilize the shell model Monte Carlo method to study the structure of rare earth nuclei. This work demonstrates the first systematic full oscillator shell with intruder calculations in such heavy nuclei. Exact solutions of a pairing plus quadrupole Hamiltonian are compared with the static path approximation in several dysprosium isotopes from $A=152$ to 162, including the odd mass $A=153$. Some comparisons are also made with Hartree-Fock-Bogoliubov results from Baranger and Kumar. Basic properties of these nuclei at various temperatures and spin are explored. These include energy, deformation, moments of inertia, pairing channel strengths, band crossing, and evolution of shell model occupation numbers. Exact level densities are also calculated and, in the case of ^{162}Dy, compared with experimental data.

PACS number(s): 21.60.Cs, 21.60.Ka, 27.70.+q, 21.10.Ma

I. INTRODUCTION

Our goal is to develop an improved microscopic understanding of the structure of rare earth nuclei, i.e., an understanding based on the behavior of individual nucleons in the nucleus. Toward that end we solve the shell model systematically in a full oscillator shell basis with intruders for the first time in rare earth nuclei using the Monte Carlo (SMMC) technique; calculations using other methods have been restricted to a severely truncated model space. SMMC allows us to trace structural rearrangements within nuclei induced by changes in temperature and spin, so that we may obtain a clearer microscopic picture of general structural features in this region of the periodic table.

We assume an effective two-body nucleon-nucleon interaction and perform a Hubbard-Stratonovich transformation to obtain a path integral representation for the partition function, which is then evaluated by Monte Carlo methods (see Sec. II) to produce an exact shell model solution within statistical errors; this substantially enhances the predictive power of the nuclear shell model for some observables. Indeed, direct diagonalizations of the shell model Hamiltonian in a full basis have been limited to $A\sim 50$, while we present calculations for $A\sim 150$.

We examine how the phenomenologically motivated pairing plus quadrupole interaction compares in exact shell model solutions vs Baranger and Kumar's HFB treatment and the static path approximation (SPA). We also examine how the model solutions compare with experimental data. There have been efforts recently by others to use SPA calculations, since it is simpler and faster. (See [1,2] as examples. Note that Rossignoli and co-workers use the SPA in the ''natural'' decomposition while the SPA here is done in the density decomposition.) In particular, it is useful to know not only if phenomenological pairing plus quadrupole type interactions can be used in exact solutions for large model spaces, but also if the parameters require significant renormalization because this affects the accuracy of the SPA.

We study a range of dysprosium isotopes ($Z=66,86\leqslant N\leqslant 96$), which exhibit a rich spectrum of the behaviors such as shape transitions, level crossings, and pair transfer that have been observed in the rare earths. These results should therefore apply quite generally in the rare earth region, although the immediate work focuses on dysprosium. We have selected this element since the half-filled proton shell makes the model spaces particularly large.

A previous paper discussed SMMC for the test case ^{170}Dy, which does not exist as a stable nucleus [3]. The work presented here is much more systematic and thorough. Algorithm improvements subsequent to [3] have increased the computational execution by a factor of 10 or more and have allowed us to calculate the rare earths at lower temperatures, nuclear shapes are calculated using the correct calculated quadrupole variance (not just a constant), and pairing operators not used in [3] are calculated.

II. THEORETICAL BACKGROUND

Shell model diagonalization is still limited to $A\sim 50$ in the $0f1p$ shell [4]. In contrast, SMMC determines thermal observables, but explicit wave functions are never constructed; this is the key to how the predictive power of the shell model is extended so tremendously. The method is far less demanding on machine storage and there is no need to perform manipulations with the exponentially increasing numbers of variables that are encountered in direct diagonalization. SMMC storage scales like $N_s^2 N_t$, where N_s is the number of single-particle shell model states and N_t is the number of time slices (see below).

No known discrepancies exist between SMMC and direct diagonalization in cases where the comparison has been possible. This includes odd mass nuclei computed for appropriate temperatures. Realistic fp and sd shell solutions using modified KB3 and Brown-Wildenthal interactions, respectively, agree with experiments [5]. These results give us a high degree of confidence in the SMMC technique.

As with any shell model, an effective nucleon-nucleon

interaction must be specified. We use the well-known pairing plus quadrupole interaction as formulated by Baranger and Kumar [6]. The Hamiltonian is

$$\hat{H}=\hat{H}_{sp}-G_p\hat{P}_p^\dagger\hat{P}_p-G_n\hat{P}_n^\dagger\hat{P}_n-\frac{\chi}{2}\hat{Q}\cdot\hat{Q} \tag{1}$$

with $\hat{Q}=\hat{Q}_p+\hat{Q}_n$. The pairing and quadrupole operators are defined as

$$\hat{P}_{J=0}^\dagger=\sum_{jm}(-)^{j-m+l}\hat{a}_{jm}^\dagger\hat{a}_{j-m}^\dagger, \tag{2}$$

$$\hat{Q}\cdot\hat{Q}=\sum_{i,j,k,l}\langle i|Q_\mu|k\rangle\langle l|Q_\mu|j\rangle\hat{a}_i^\dagger\hat{a}_j^\dagger\hat{a}_l\hat{a}_k, \tag{3}$$

where $Q_\mu=r^2Y_{2\mu}(\theta,\phi)$ as usual. The single-particle energies are also taken from Baranger and Kumar [6].

Effective charges are incorporated to account for core polarization to fit measured electric quadrupole transition strengths. The electric quadrupole operator, with effective charges e_p and e_n, is

$$\hat{Q}=e_p\hat{Q}_p+e_n\hat{Q}_n. \tag{4}$$

A. Method and sign problem

Detailed procedures for the SMMC are explained fully in [5] and references therein. We provide no further explanation, except as regards the ''sign problem.''

We define $\Phi\equiv\mathrm{Tr}\,\hat{U}_\sigma/|\mathrm{Tr}\,\hat{U}_\sigma|$ as the sign for a given Monte Carlo sample, where $\hat{U}_\sigma$ is defined as

$$\hat{U}_\sigma=\hat{U}_{N_t}\hat{U}_{N_t-1}\cdots\hat{U}_1, \tag{5}$$

$$\hat{U}_n=e^{-\Delta\beta\hat{h}_\sigma}. \tag{6}$$

$\hat{h}_\sigma$ is the one-body Hamiltonian for the auxiliary field configuration σ and β is the inverse temperature. In SMMC, the partition function path integral is divided into N_t time steps of size $\Delta\beta$ so that $\beta=N_t\Delta\beta$. Hence, the complete evolution operator is expressed as a product of operators in each time step. In these studies, we use the canonical (number projection) formalism to evaluate the trace.

If Φ is not equal to 1, numerical instabilities can arise. This has become widely known as the Monte Carlo ''sign problem.'' The simple phenomenological pairing plus quadrupole interaction (without added pn pairing) does not have an inherent sign problem. However, sign problems can arise even with this simple interaction if time-reversal symmetry is broken, as when odd masses are studied or the system is cranked by adding a term $-\omega\hat{J}_z$ to $\hat{H}$. In these studies, the sign violation turned out to be minor for odd mass ground states and canonical ensemble cranking was limited to $\omega\leqslant 0.3$ MeV. Experimentally, these nuclei are observed to $\omega\approx 0.6$ MeV [7].

B. Shapes and moments of inertia

The quadrupole expectation values $\langle Q_\mu\rangle$ vanish under rotational symmetry. However, for a given Monte Carlo sample Q_μ will have some finite, nonzero value. We calculate $Q_{ij}=3x_ix_j-\delta_{ij}r^2$ for each sample and relate its eigenvalues to the quadrupole β and γ deformation parameters, as done previously with SMMC [8,3]. The intrinsic frame for each sample with a field configuration σ has nonzero components Q_0' and $Q_2'=Q_{-2}'$ as

$$\langle Q_0'\rangle_\sigma=\frac{3}{2\pi}\sqrt{\frac{4\pi}{5}}\langle r^2\rangle_\sigma\beta_\sigma\cos\gamma_\sigma,$$

$$\langle Q_2'\rangle_\sigma=\frac{3}{2\pi}\sqrt{\frac{4\pi}{5}}\langle r^2\rangle_\sigma\frac{\beta_\sigma}{\sqrt{2}}\sin\gamma_\sigma. \tag{7}$$

In terms of eigenvalues Q_{11}', Q_{22}', and Q_{33}' of Q_{ij} give

$$\langle Q_{11}'\rangle_\sigma=\sqrt{\frac{2\pi}{5}}[\sqrt{3}[\langle Q_2'\rangle_\sigma+\langle Q_{-2}'\rangle_\sigma)-\sqrt{2}\langle Q_0'\rangle_\sigma],$$

$$\langle Q_{22}'\rangle_\sigma=\sqrt{\frac{2\pi}{5}}[-\sqrt{3}(\langle Q_2'\rangle_\sigma+\langle Q_{-2}'\rangle_\sigma)-\sqrt{2}\langle Q_0'\rangle_\sigma],$$

$$\langle Q_{33}'\rangle_\sigma=2\sqrt{\frac{4\pi}{5}}\langle Q_0'\rangle_\sigma.$$

We can also calculate the free energy $F(\beta,\gamma)$ to construct shape contour plots. This is done using

$$F(\beta,\gamma)=-T\ln\frac{P(\beta,\gamma)}{\beta^3\sin 3\gamma}. \tag{8}$$

$P(\beta,\gamma)$ is the shape distribution as a function of the deformation coordinates (β,γ) and T is the temperature. Plots are truncated at small γ for an obvious reason. All shape plots discussed in this paper are for the mass quadrupole and are not for electric quadrupoles.

Moments of inertia are calculated in the cranked Hamiltonian ($\hat{H}\rightarrow\hat{H}-\omega\hat{J}_z$) using $\mathcal{I}_2=d\langle\hat{J}_z\rangle/d\omega$. We expect moments of inertia to initially increase as the nucleus is cranked and then to decrease when pairs are broken.

C. Pairing composition

Pairing correlations in nuclei can be studied by calculating pairing strengths in different spins for protons and neutrons. For like particle pairs, define the pair creation operator as

$$A_{JM}^\dagger=\frac{1}{\sqrt{1+\delta_{ab}}}[\hat{a}_{j_a}^\dagger\times\hat{a}_{j_b}^\dagger]_{JM}(-)^{l_b} \tag{9}$$

where

$$[\hat{a}_{j_a}^\dagger\times\hat{a}_{j_b}^\dagger]_{JM}=\sum_{m_a,m_b}(j_am_aj_bm_b|JM)\hat{a}_{j_a}^\dagger\hat{a}_{j_b}^\dagger. \tag{10}$$

Note that we consider only like particle pairing, i.e., proton-proton and neutron-neutron [Eq. (1)]. Now let $\alpha=(j_a,j_b)$ and $\alpha'=(j_c,j_d)$. Using the pair creation operator, a matrix $M^J_{\alpha,\alpha'}$ can be constructed as

$$M^{J\pi}_{\alpha,\alpha'}=\sum_M \langle A^\dagger_{JM}(j_a,j_b)A_{JM}(j_c,j_d)\rangle, \tag{11}$$

from which we can then define a pairing strength P^J as

$$P^{J\pi}=\sum_{\alpha\geqslant\alpha'} M^{J\pi}_{\alpha,\alpha'}. \tag{12}$$

The correlated pair strength, which is more useful, is obtained by subtracting uncorrelated mean field pairs from the total $P^{J\pi}$ defined above. A Fermi gas has generally been used for the mean field with SMMC. Letting $n_k=\langle \hat{a}^\dagger_k \hat{a}_k\rangle$ and substituting $n_2n_1(\delta_{23}\delta_{14}-\delta_{24}\delta_{13})$ for $\langle \hat{a}^\dagger_1\hat{a}^\dagger_2 a_3 a_4\rangle$ in Eq. (11) yields the Fermi gas mean field pair strength $P^{J\pi}_{MF}$. In this case, of course, we could use the SPA occupations as the ''mean field'' to subtract from the complete pairing plus quadrupole solutions.

Even-even nuclei have correlated ground states, so we expect an excess of $J=0$ pairs beyond the mean field in even-even ground states. The hallmark for a pair condensate is the existence of one eigenvalue of $M^{J\pi}_{\alpha,\alpha'}$ that is much greater than all the rest.

The pair matrix can be diagonalized to find the eigenbosons $B^\dagger_{\alpha JM\pi}$ as

$$B^\dagger_{\alpha JM\pi}=\sum_{ab} \psi_{\alpha JM\pi}(ab)A^\dagger_{JM\pi}(ab), \tag{13}$$

where $\alpha=1,2,\ldots$ labels the various bosons with the same angular momentum and parity. The $\psi_{\alpha J\pi}$ are the eigenvectors of the diagonalization, i.e., the wave functions of the boson, and satisfy the relation

$$\sum_{j_aj_b} \psi^*_{\alpha J\pi}\psi_{\mu J\pi}=\delta_{\alpha\mu}. \tag{14}$$

These eigenbosons satisfy

$$\sum_M \langle B^\dagger_{\alpha JM\pi}B_{\gamma JM\pi}\rangle = n_{\alpha J\pi}\delta_{\alpha\gamma}, \tag{15}$$

where the positive eigenvalues $n_{\alpha J\pi}$ are the number of $J\pi$ pairs of type α.

D. Backbending

We can monitor the pair strength for neutrons coupled to $J=12$ as a signature for the anticipated band crossing or backbending. The only orbital in our model space that can produce this coupling is the neutron $i_{13/2}$ level. We do not monitor backbending by mapping out the typical backbending plot of I vs ω because the backbend in the plot requires a multivalued solution of I, whereas SMMC always produces a single-valued solution from the statistical ensemble.

E. Level density in shell model Monte Carlo

SMMC is an excellent way to calculate level densities. $E(\beta)=\langle\hat{H}\rangle$ is calculated for many values of β, which then determines the partition function Z as

$$\ln[Z(\beta)/Z(0)]=-\int_0^\beta d\beta' E(\beta'); \tag{16}$$

$Z(0)$ is the total number of available states in the space. The level density is then computed as an inverse Laplace transform of Z. Here, the last step is performed with a saddle point approximation:

$$S(E)=\beta E+\ln Z(\beta), \tag{17}$$

$$\rho(E)=(2\pi\beta^{-2}C)^{-1/2}\exp(S), \tag{18}$$

where $\beta^{-2}C\equiv -dE/d\beta$. SMMC has been used recently to calculate level densities in iron region nuclei [9]. Here, we present the first exact level density calculation for the much heavier Dy.

Nuclear level densities in the static path approximation have previously been investigated by Alhassid and Bush for a simple solvable Lipkin model [10]. The simple Lipkin Hamiltonian does not include pairing, however. These authors found the SPA to be superior to the mean field approximation and the difference between the two depended on interaction strength.

F. Recap on interaction and model space

It is fortunate that the elementary pairing plus quadrupole interaction does not break the Monte Carlo sign so that no g extrapolation is required. The calculation of level densities is also simplified, since accurate results require very low statistical uncertainties [9].

We do not include isovector proton-neutron (pn) pairing in the interaction. This is a reasonable assumption since fp shell calculations with SMMC have shown clearly that isovector pn correlations diminish quickly as N exceeds Z and we are not at $N\sim Z$ [11]. Further, in our case the valence protons and neutrons occupy different oscillator shells. To be sure, some pn correlations are included via the isoscalar quadrupole interaction ($2\hat{Q}_p\cdot\hat{Q}_n$), but any observable that depends strongly on pn correlations such as the Gamow-Teller strength will not be accurately determined with this interaction.

We chose one shell each for protons (sdg) and neutrons (pfh) with the opposite parity intruders $h_{11/2}$ and $i_{13/2}$, respectively. The space encompasses 32 proton levels and 44 neutron levels. The oscillator length, $b=\sqrt{\hbar/m\omega_0}$, was taken to be $1.01A^{1/6}$ fm.

With this space, Dy has sixteen valence protons so that the proton shell is half filled. The number of valence neutrons varies from four in ^{152}Dy to fourteen in ^{162}Dy. This model space is identical to the one used by Kisslinger and Sorensen [12], but is smaller than the two-shell space Baranger and Kumar used.

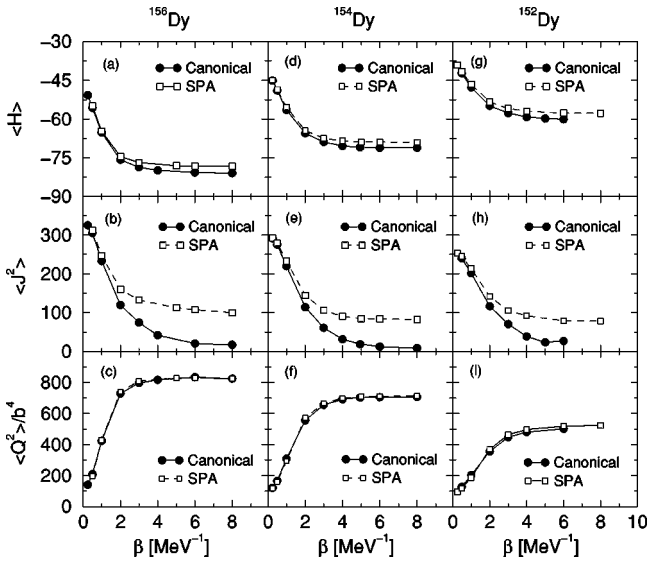

FIG. 1. (a)–(c) Energy, spin, and quadrupole moment for ^{156}Dy. (d)–(f) Energy, spin, and quadrupole moment for ^{154}Dy. (g)–(i) Energy, spin, and quadrupole moment in ^{152}Dy.

We have also done some calculations in a larger space including the unique-parity orbits below our original model space ($g_{9/2}$ for protons and $h_{11/2}$ for neutrons). These results are discussed last.

G. Static path approximation and mean field

The static path approximation is the one-time-slice limit of the partition function path integral and is obviously easily implemented in SMMC. The mean field approximation is the saddle point estimation of the path integral; neither includes imaginary time-dependent terms. The SPA differs from mean field since the integral over time-independent auxiliary fields in the SPA is done exactly, so that contributions from multiple configurations (even with large fluctuations) are included rather than just the single, steepest-descent mean field.

Static path calculations do not do as well with realistic interactions as with schematic interactions, e.g., pairing plus quadrupole. Also, the accuracy of the approximation varies among operators, as will be demonstrated in Sec. III.

III. RESULTS

A. Static path approximation versus full solution: Static properties

1. Energy, spin, and quadrupole moments

Comparisons of the SPA and full path solutions for the static observables energy $\langle H\rangle$, spin $\langle J^2\rangle$, and mass quadrupole moment $\langle Q^2\rangle$ are shown for the experimentally deformed, transitional, and spherical isotopes in Figs. 1(a)–1(i). A few of the full canonical calculations do not extend quite as low in temperature as the SPA results due to numerical instability developing from multiple matrix multiplications. Error bars in these plots are smaller than the dot sizes and are therefore not shown. Also, note that the quadrupole moments are expressed as $\langle Q^2\rangle/b^4$, where b is the oscillator length.

The SPA energy is greater than the exact energy, except at very high temperatures, for all three of these nuclei; at the lowest temperatures, the difference is a few MeV. The origin of this discrepancy will be discussed below (Sec. III A 2). The difference between SPA and exact canonical ground state energies is 2.39 ± 0.15 MeV for ^{152}Dy and 2.59 ± 0.18 MeV for ^{156}Dy, so there is not a significant discrepancy between the lighter and heavier isotopes. Thus, the SPA does not predict absolute energies accurately, but works well for relative differences. The partition function integral in SMMC is always divided into time steps of fixed size $\Delta\beta$, which is fixed at 0.0625 MeV^{-1}. As the temperature $1/\beta$ increases the number of time slices in the exact partition function expression decreases. Hence, it is not surprising that the SPA is more accurate for higher temperatures.

Looking at $\langle J^2\rangle$ shows that the SPA calculations only cool to about $J=8-10$ for even the lowest calculated temperatures, while the even-even ground states are, of course, $J=0$. In these canonical SMMC calculations, $J=0$ is not exactly reached even in the full canonical calculations because the thermal ensemble always includes contributions from higher energy states. An estimate for the β required for good filtering to the even-even ground states is $\beta=1/E(2_1^+)$, where $E(2_1^+)$ is the measured energy of the first 2^+ state. This β value varies from $\beta=1.6$ MeV^{-1} for ^{152}Dy to $\beta=11.5$ MeV^{-1} for ^{162}Dy as $E(2_1^+)$ varies from 0.614 to 0.087 MeV.

The thermal spin expectation $\langle J^2\rangle$ can, in principle, be compared against the experimental spectra. However, one never experimentally knows all the states in a nucleus so such a direct comparison is difficult except at low excitation energies, which are dominated by the well-known ground state band. The difference in $\langle J^2\rangle$ between SPA and full canonical solutions at the lowest temperatures is 58 for ^{152}Dy, 74 for ^{154}Dy, and 91 for ^{156}Dy. Hence, the deviation is worse with increasing deformation in these isotopes.

The SPA works very well for the quadrupole moments. This result is also very robust, i.e., strengthening or weakening the coupling χ beyond the nominal Baranger-Kumar value does not affect the agreement between SPA and exact results.

More information about the static quadrupole moment appears in Figs. 2(a)–2(d), where the proton and neutron quadrupole components are shown separately. The neutron quadrupole moment increases quickly from ^{152}Dy to ^{154}Dy and increases much more slowly after the onset of deformation in ^{156}Dy. The proton quadrupole moment, meanwhile, remains approximately fixed for all the isotopes studied. $\langle Q_v^2\rangle$ increases rapidly as A increases from 154 to 162. Relative to $\langle Q^2\rangle$ it is only 8.5% [Fig. 2(a)], but the total quadrupole moment at $\beta=6$ MeV^{-1} is 46% larger for ^{162}Dy than for ^{156}Dy ($1221b^4$ vs $834b^4$). $\langle Q_v^2\rangle/\langle Q^2\rangle$ is roughly 10% for all isotopes, where Q_v is the isovector quadrupole operator (Q_p-Q_n).

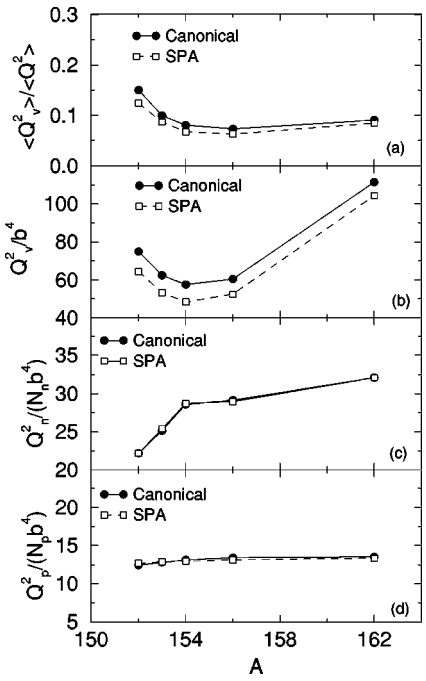

FIG. 2. SPA and exact canonical solutions for quadrupole observables in selected dysprosium isotopes $A=152$ to $A=162$. All results are for $\beta=6$ or $T=0.167$ MeV. $\langle Q_v^2\rangle$ is defined as $(Q_p-Q_v)^2$ and b is the oscillator length.

Another comparison between SPA and full canonical calculations is how quickly the solutions cool for various observables. For example, in ^{152}Dy $\langle H\rangle$ appears to have stabilized by $\beta=6$ MeV^{-1} in both the SPA and the full solution. The spin $\langle J^2\rangle$ and quadrupole moment $\langle Q^2\rangle$ also appear to have minimized near $\beta=6$ MeV^{-1} in the SPA and exact calculations. Similar results are evident in the other nuclei, except for $\langle J^2\rangle$ in ^{156}Dy, which is clearly decreasing still in the SPA for $\beta=8$ MeV^{-1}, the largest value for which the calculation could be done.

2. Pairing energy and gaps

Some insight can be had by looking at the pairing energy and gaps. The quadrupole energy, $-0.5\chi\langle\hat{Q}\cdot\hat{Q}\rangle$ in the SPA agrees well with the full canonical solution, but the total energies in the SPA shown above have clear deviations from the exact canonical results. The difference in $\langle H\rangle$ is due to the pairing energy. The accuracy of the SPA in the pairing interaction depends strongly on the pairing strength and is naturally better for weaker pairing.

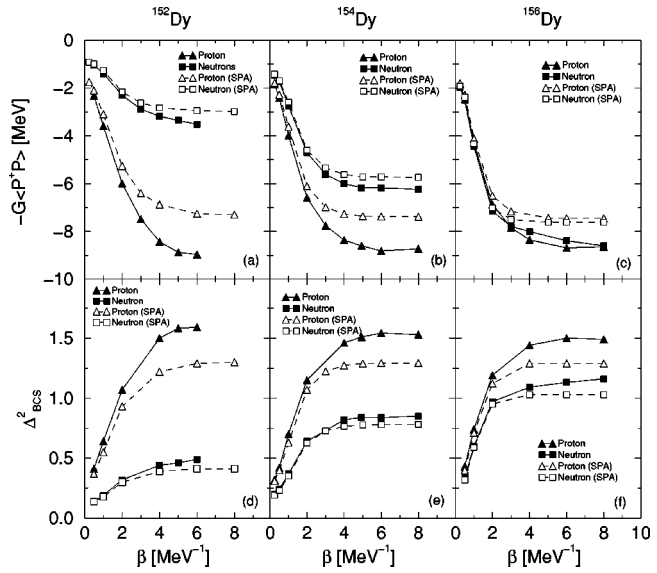

FIG. 3. Pairing energy in ^{152}Dy (a), ^{154}Dy (b), and ^{156}Dy (c). BCS pair gaps are shown for ^{152}Dy (d), ^{154}Dy (e), and ^{156}Dy (f).

The pairing energies and BCS pair gaps for $^{152-156}$Dy are shown in Figs. 3(a)–3(f). The latter were obtained from the pairing energies by $\Delta_{BCS}^2/G=H_{pair}$. The disagreement between SPA and exact calculations looks worse for protons, but recall that there are 16 valence protons and just 4–8 valence neutrons in these isotopes.

B. $B(E2)$ and effective charges

The reduced electric quadrupole transition strength $B(E2)$ is computed from

$$B(E2)=\langle(e_p\hat{Q}_p+e_n\hat{Q}_n)^2\rangle, \tag{19}$$

where e_p and e_n are effective proton and neutron charges. We have taken $e_p=1+x, e_n=x$. Results are shown in Table I and Fig. 4, where it has been assumed that the total $B(E2)$ calculated in SMMC is the same as $B(E2;2_1^+\rightarrow 0_1^+)$. Effective charges in column 3 and column 4 are fitted to measured $B(E2)$ values. Typical effective charges in rare earths are approximately $e_{p(n)}=2(1)$, so these values are in a reasonable range.

TABLE I. SMMC $B(E2)$ vs measured $B(E2;2_1^+\rightarrow 0_1^+)$ with specified effective charges. $B(E2)$ in W.u. Errors are statistical Monte Carlo sampling errors. Column 6, $B(E2)$ for SMMC/BK $e_p(n)$, is the $B(E2)$ obtained from SMMC calculated quadrupole moments with Baranger-Kumar effective charges.

A	N	e_p	e_n	$B(E2)$ SMMC	$B(E2)$ SMMC/BK $e_{p(n)}$	$B(E2)$ Expt.
152	86	1	0	13±0.2	N/A	13
154	88	1.5	0.5	97±0.2	N/A	97
156	90	1.75	0.75	146±0.6	126.4±0.5	146
162	96	1.75	0.75	199±0.7	150.1±0.5	199

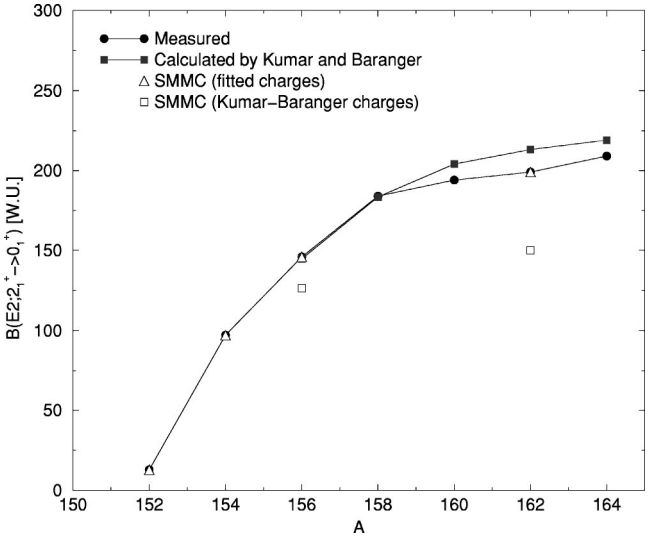

FIG. 4. SMMC results for $B(E2;2_1^+ \rightarrow 0_1^+)$ for dysprosium isotopes. Results also shown in deformed cases ($A=156$, $A=162$) for strengths calculated with SMMC quadrupole moment and Baranger-Kumar effective charges.

Table I and Fig. 4 also show what $B(E2)$ strength would be obtained from SMMC quadrupole moments with Baranger-Kumar charges. This illustrates how a small change in the effective charge can produce a comparatively large change in the $B(E2)$. For ^{162}Dy, the 7% difference in e_p when using Baranger-Kumar charges leads to a 23% change in $B(E2)$.

The collectivity of a nucleus, and thus the $B(E2)$ value, varies with the energy $E(2_1^+)$. The effective proton charge e_p is plotted against $E(2_1^+)$ in Fig. 5. For the SMMC results, the neutron effective charge needs to be zero for spherical

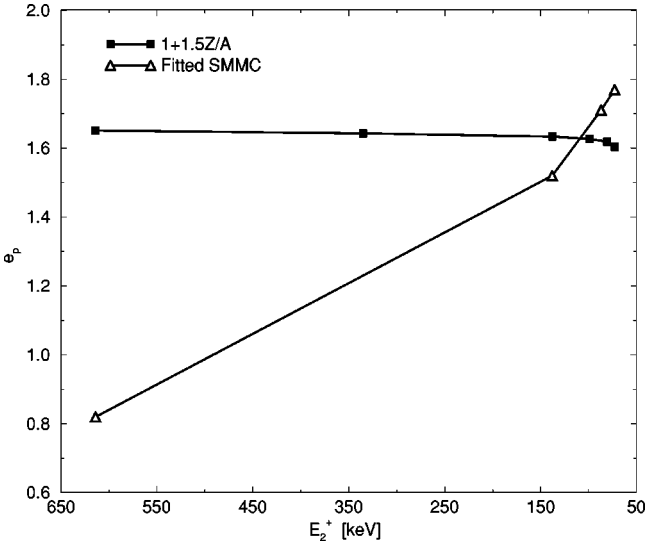

FIG. 5. Effective charge vs $E(2_1^+)$ in Dy. Shown for Baranger-Kumar effective charge in deformed nuclei, $e_p=1+1.5Z/A$, and fitted SMMC charges. $E(2_1^+)=614$ keV is spherical ^{152}Dy and $E(2_1^+)=335$ keV is ^{154}Dy. The other points are for deformed ^{156}Dy and ^{162}Dy.

TABLE II. Some spherical $E(2_1^+)$ values from Baranger-Kumar [6]. Energies in keV.

	$E(2_1^+)_{\text{expt}}$	$E(2_1^+)_{\text{theor}}$
^{138}Ba	1438	2767
^{140}Ba	602	2006
^{140}Ce	1596	2531
^{142}Ce	641	1772
^{144}Ce	397	1095

^{152}Dy to avoid severely overestimating the $B(E2;2_1^+ \rightarrow 0_1^+)$ strength as it is calculated above. The fitted effective charge is $e_p=1.75$ for the deformed isotopes and it is intermediate for ^{154}Dy. This is a reflection of the fact that exact solutions for the mean field interaction yield lighter dysprosiums which are too deformed (Sec. III E); the effective charge should be constant.

It should be noted that Baranger and Kumar did not calculate $B(E2)$ values for spherical nuclei in the same way as for deformed nuclei, i.e., they did not take effective charges for spherical nuclei as $e_p=1+1.5Z/A$, $e_n=1.5Z/A$. For spherical nuclei, they combined phonon and rotational model properties (see [6], p. 552). They used $E(2_1^+)=(C/B)^{1/2}$ and $B(E2,0\rightarrow 2)\propto Z^2R_0^4(BC)^{-1/2}$ from the phonon model with the relation $Q_s\propto B(E2)^{1/2}$. These $E(2_1^+)$ predictions are not very good (Table II).

C. Static path approximation versus full solution: Cranking

1. Sign limits on cranking

Recall from Sec. II A that cranking degrades the Monte Carlo sign from unity and that calculations become impractical when the sign drops below 0.5. This is illustrated for both full canonical and SPA results for ^{156}Dy in Figs. 6(a) and 6(b). Error bars are not displayed in these figures since they are small; the statistical error in Φ for $\beta=6$ MeV^{-1} and $\omega=0.3$ MeV is 0.04. Canonical cranking in this nucleus is limited to small frequencies for $\beta=8$ MeV^{-1}, as evidenced by the quick drop in sign from $\omega=0.05$ MeV to ω

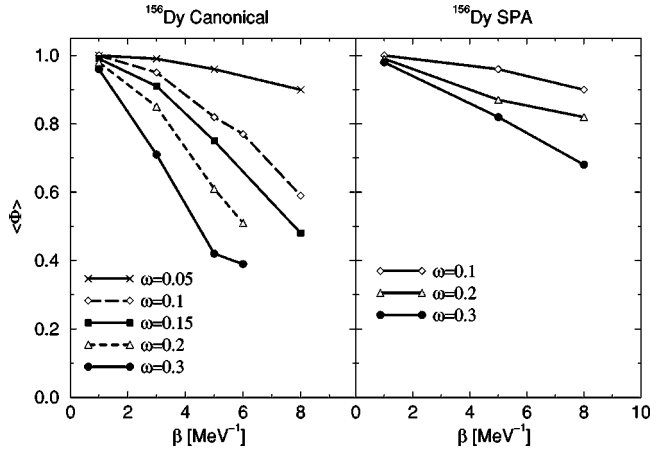

FIG. 6. Monte Carlo sign for canonical (a) and SPA (b) cranking in ^{156}Dy.

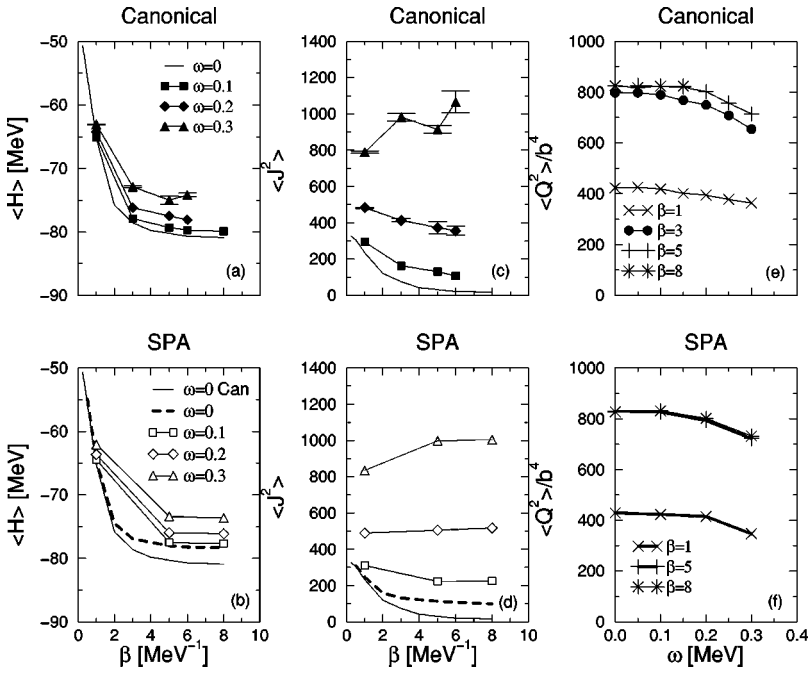

FIG. 7. Canonical vs SPA cranking results in ^{156}Dy for energy (a) and (b), spin (c) and (d), and quadrupole moment (e) and (f). Error bars are not shown for SPA results since they are smaller than the symbols.

$=0.1$ MeV. The canonical cranking is fairly good for $\beta \leqslant 6$ MeV^{-1}, especially $\beta \leqslant 4$ MeV^{-1}. SPA cranking predictably has better sign properties. In the SPA, ^{156}Dy can be cranked well out to $\beta=8$ MeV^{-1}, which is the approximate limit of temperature that can be reached in this nucleus without matrix stabilization.

2. Energy, spin, and quadrupole moments again

Energy, spin, and quadrupole moments at various temperatures are compared at different cranking frequencies in exact canonical and SPA methods. Calculations for ^{156}Dy appear in Figs. 7(a)–7(f). Energy results for the SPA at different cranking frequencies mirror the full canonical result. In the range $5 \leqslant \beta \leqslant 8$ MeV^{-1}, or $0.2 \leqslant T \leqslant 0.125$ MeV, $\omega=0.1$ MeV lies at small excitation energy ϵ above the $\omega=0$ baseline, $\omega=0.2$ MeV lies roughly 3ϵ above the baseline, and $\omega=0.3$ MeV is excited by approximately 6ϵ above $\omega=0$.

The spin results reveal that $\langle J^2 \rangle$ in the SPA is higher than the exact canonical result until $T \geqslant 1$ MeV when $\omega \leqslant 0.2$ MeV. However, for $\omega=0.3$ MeV, the SPA agrees well with the exact solution. The exact solution is not shown for $\beta=8$ MeV^{-1} at this frequency due to numerical difficulties. The SPA $\langle J^2 \rangle$ for $\omega=0.2$ MeV is very flat across the computed temperature range, $0.125 \leqslant T \leqslant 1$ MeV. As with the exact solution, $\langle J^2 \rangle$ decreases with rising temperature for $\omega=0.3$ MeV.

Quadrupole results with cranking are similar to the $\omega=0$ results in that the quadrupole moment does not change when the temperature is decreased below 200 keV at any frequency studied here. Note that the quadrupole results are plotted vs ω for various temperatures. At the lowest temperatures, the quadrupole moment begins to decrease after $\omega=0.15$ MeV in the canonical case. It decreases after $\omega=0.1$ MeV in the SPA; however, $\omega=0.15$ MeV is not computed there so it is difficult to say if the quadrupole moment is declining at frequency 0.1 or 0.15 MeV in the SPA. The SPA agrees very well with the exact solution for $\langle Q^2 \rangle$ at all temperatures and cranking frequencies computed.

3. Moments of inertia

The J_z variation with cranking frequency determines the moment of inertia. Results for ^{156}Dy are displayed in Figs. 8(a) and 8(b) for both canonical and SPA cases.

The moment of inertia $\mathcal{I}_2$ for ^{156}Dy is 44.6 ± 7 $\hbar^2$/MeV in the exact canonical ensemble at $J \approx 4$ with $\beta=8$ MeV^{-1} and is 73.0 ± 2 $\hbar^2$/MeV at the same ω in the SPA. At this temperature, $T=0.125$ MeV, the SPA moment

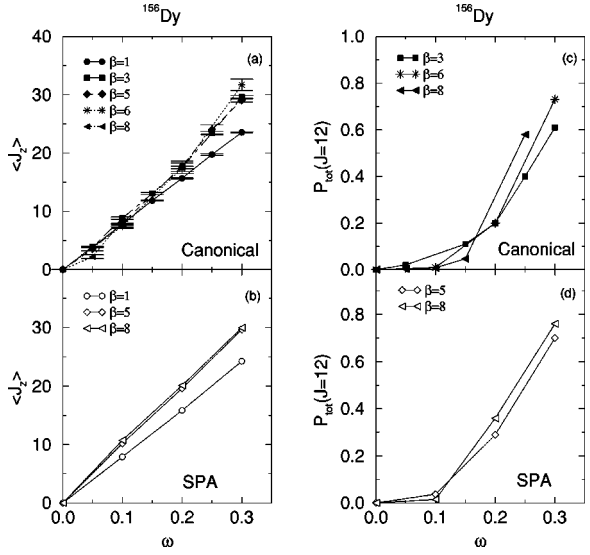

FIG. 8. (a) and (b) $\langle J_z \rangle$ for canonical and SPA cranking in ^{156}Dy. (c) and (d) $J=12$ pair strength in canonical and SPA cranking in ^{156}Dy. $J=12$ pair strength comes exclusively from $i_{13/2}$.

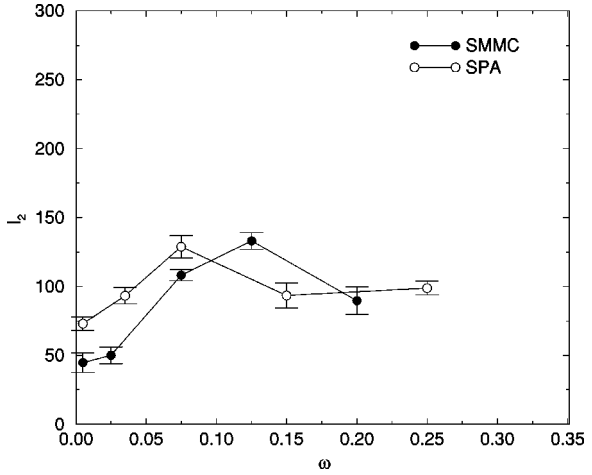

FIG. 9. SMMC vs SPA moment of inertia in ^{156}Dy. Moment of inertia is in units $\hbar^2$/MeV.

of inertia is 64% larger than the exact result. The experimental moment of inertia $\mathcal{I}_2 = 40\ \hbar^2$/MeV at $J=4$, which matches the SMMC canonical result. Also, the rigid body moment of inertia for ^{156}Dy with $(\beta,\gamma)=(0.24,0)$ is 73 $\hbar^2$/MeV. This coincides with the SPA moment of inertia.

The moment of inertia as a function of frequency is plotted in Fig. 9. As discussed in Sec. II D, the moment of inertia calculated with SMMC in a backbending region can be misleading because SMMC cannot produce a multivalued solution. As discussed in the next section, the band crossing occurs around $\omega=0.15$ in the full canonical ensemble calculation. From Fig. 9, we see that the moment of inertia peaks near $\omega=0.125$ in SMMC and peaks at slightly lower spin near $\omega=0.075$ in the SPA.

D. Band crossing

The pairing strength for $J=12$ pairs in ^{156}Dy, which can be produced only from $i_{13/2}$ neutron pairs, is shown in Figs. 8(c) and 8(d). The strength $P_{J=12}$ begins to increase quickly in the canonical case for $(\beta,\omega)=(8,0.15)$, which corresponds to $J=16\pm1$. In the SPA, $P_{J=12}$ increases sharply beyond $(\beta,\omega)=(8,0.1)$, which corresponds to $J=14$. The increasing $J=12$ pair strength coincides with declining moment of inertia (Fig. 9).

The occupations of both the proton $h_{11/2}$ and neutron $i_{13/2}$ intruder orbitals for ^{156}Dy are given in Figs. 10(a) and 10(b). The proton intruder occupation is comparatively stable over this same spin range at each temperature. However, it is clear that the $i_{13/2}$ occupation is increasing with spin, particularly for lower temperatures, as expected. The $h_{11/2}$ occupation number decreases slightly with temperature for all frequencies computed. Occupation shifts slightly to $\pi d_{5/2}$. For $\beta=6$ MeV^{-1}, the maximum spin J_z corresponds to $J\approx32$ and for $\beta=1$ MeV^{-1}, the maximum spin is $J\approx28$. Unfortunately for $\beta=6$ MeV^{-1}, or $T=167$ keV, the Monte Carlo sign is reduced to 0.4 at the maximum spin shown (recall Fig. 6). At $\beta=1$ MeV^{-1}, however, the sign is still very stable at 0.96.

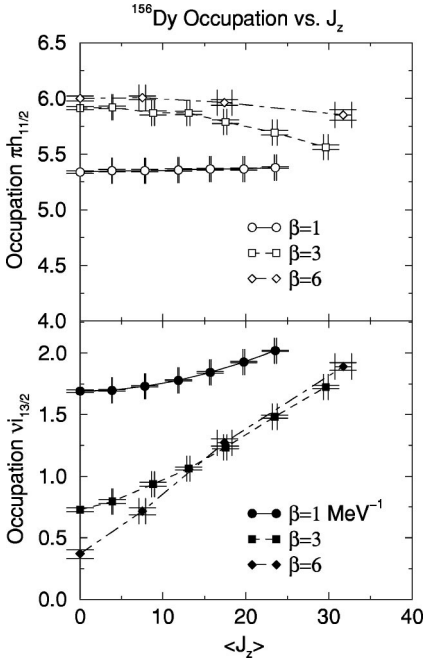

FIG. 10. Occupation for proton $h_{11/2}$ (a) and neutron $i_{13/2}$ (b) vs spin.

E. Shape versus temperature and spin

Nuclear shapes have also been computed to clarify how the shape varies with temperature and spin. Temperatures and frequencies for these calculations are given in the figure captions. In all shape graphs, the β axis is radial and the other axis is the γ axis. Results for ^{152}Dy at temperatures from $T=0.25$ MeV to $T=2$ MeV are shown in Fig. 11.

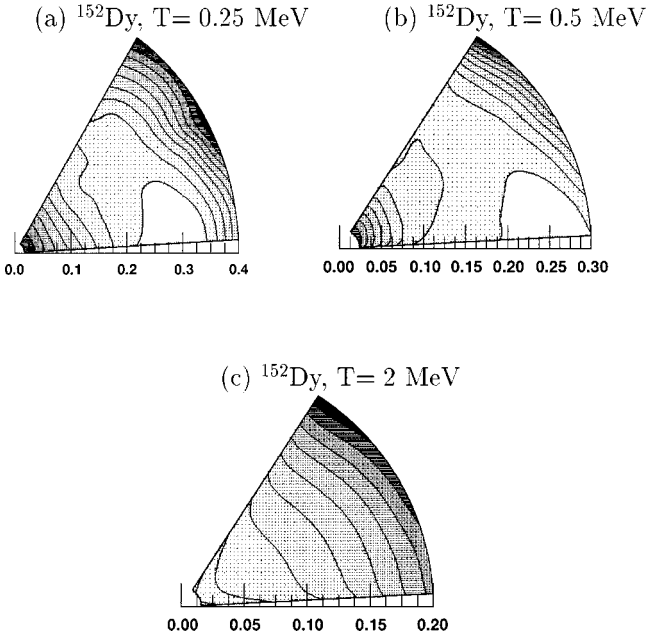

FIG. 11. (a) Shape at $T=0.25$ MeV for ^{152}Dy. Contour spacing is 0.79 MeV. (b) Shape at $T=0.5$ MeV for ^{152}Dy. Contour spacing is 0.64 MeV. (c) Shape at $T=2$ MeV for ^{152}Dy. Contour spacing is 2.9 MeV. Each plot is compiled from 2000 samples.

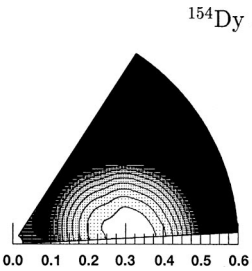

FIG. 12. Shape at $T=0.133$ MeV for ^{154}Dy from 4800 samples. Contour spacing is 0.92 MeV.

The nucleus becomes increasingly spherical for rising temperature.

Shapes for ^{154}Dy and ^{156}Dy are shown in Figs. 12–14. These were all produced from the exact canonical ensemble except Fig. 13(f), which was produced with the static path approximation. Cranked contour plots, such as Fig. 14(d) for ^{156}Dy at $(\beta,\omega)=(8,0.1)$, show the nuclei becoming increasingly gamma-soft with increasing spin. This is also true in the SPA [Fig. 13(f)], which was utilized in this case since the Monte Carlo sign for the exact calculation becomes too small to obtain useful results. There is no sign of oblate shape at this spin in ^{154}Dy, as predicted by Cranmer-Gordon *et al.* using a Nilsson-Strutinsky cranking model [13]. However, the SMMC ground state deformation in ^{154}Dy with these parameters is clearly too large. Ma *et al.* [14] claimed evidence for a return to some collectivity in ^{154}Dy from spin 36^+ to 48^+. The shape plot for ^{154}Dy at $J\sim 50$ [Fig. 13(f)] appears soft. The SMMC $B(E2)=5$ W.u. at this spin using the fitted effective charge.

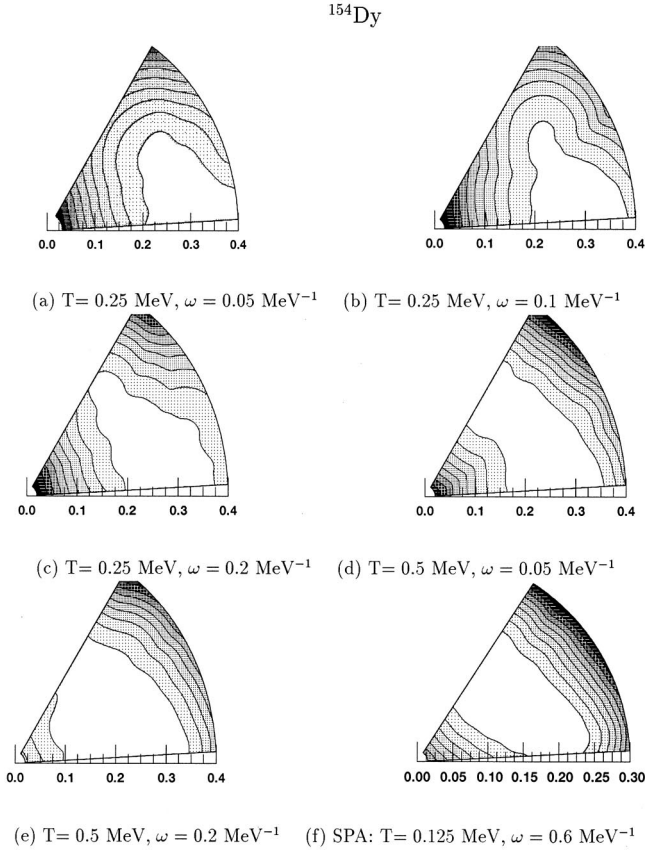

FIG. 13. (a) Shape at $T=0.25$ MeV and $\omega=0.05$ ($J\approx 6$) for ^{154}Dy. 2560 samples. Contour spacing is 2.9 MeV. (b) Shape at $T=0.25$ MeV and $\omega=0.1$ ($J\approx 8$) for ^{154}Dy. 2400 samples. Contour spacing 2.5 MeV. (c) Shape at $T=0.25$ MeV and $\omega=0.2$ for ^{154}Dy. 2400 samples. Contour spacing 2.4 MeV. (d) Shape at $T=0.5$ MeV and $\omega=0.05$ ($J\approx 10$) for ^{154}Dy. 3840 samples. Contour spacing 3.4 MeV. (e) Shape at $T=0.5$ MeV and $\omega=0.2$ ($J\approx 20$) for ^{154}Dy. 1920 samples. Contour spacing 4.2 MeV. (f) Shape at $T=0.125$ MeV and $\omega=0.6$ ($J\approx 50$) for ^{154}Dy in SPA. Sign $\Phi=0.5$. 2000 samples. Contour spacing 1.2 MeV.

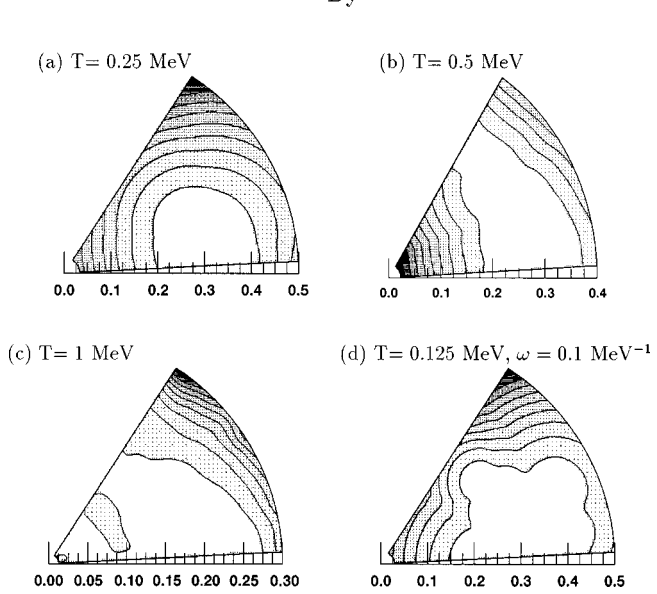

FIG. 14. (a) Shape at $T=0.25$ MeV for ^{156}Dy. 2000 samples. Contour spacing is 6.5 MeV. (b) Shape at $T=0.5$ MeV for ^{156}Dy. 2000 samples. Contour spacing is 6.9 MeV. (c) Shape at $T=1$ MeV for ^{156}Dy. 2000 samples. Contour spacing is 2.0 MeV. (d) Shape at $T=0.125$ MeV for ^{156}Dy with $\omega=0.1$ MeV^{-1}. 4800 samples. Contour spacing is 3.0 MeV.

Note that with increasing A in these isotopes, the ground state deformation is roughly constant and the depth of the minimum increases. In fact for ^{156}Dy, the depth of the well is roughly the same as the fission barrier ($\sim$40 MeV) [15]. The very low temperature results for ^{156}Dy and ^{162}Dy (not shown) do not coincide with the mean field.

Previously published shape plots from SMMC results in gamma-soft nuclei using a pairing plus quadrupole Hamiltonian with quadrupole pairing [16] did not exhibit this. However, those nuclei are only weakly deformed ($\beta\approx 0.05$–0.15) while the dysprosiums with $A\geqslant 154$ are well deformed ($\beta\approx 0.3$). For the dysprosium shapes in this paper, the unexpected depth of the potential well is evident only for well-deformed cases.

It is apparent from the above that the dysprosiums are all deformed in their ground states in the exact model calculation. However, ^{152}Dy is known experimentally to be spherical. Baranger and Kumar did not calculate ^{152}Dy, though they did calculate some other spherical isotopes. A shape plot has also been constructed from SMMC results in ^{140}Ba

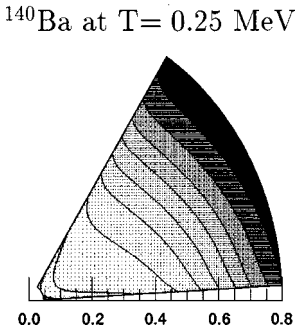

FIG. 15. Shape at $T=0.25$ MeV for ^{140}Ba. 4000 samples. Contour spacing 0.42 MeV.

for comparison with Baranger and Kumar (Fig. 15). The SMMC result for ^{140}Ba agrees with the Baranger-Kumar result; both calculations indeed show a spherical nucleus. This isotope has $Z=56$ and $N=84$. For the shell model space used, this becomes six valence protons and two valence neutrons so that, unlike dysprosium, the proton shell is less than half filled. The SMMC $B(E2;2\rightarrow0)$ is 5 W.u. using the effective charge fitted for the dysprosiums. Reducing the quadrupole coupling to half its mean field strength still yielded deformation $\beta\approx0.3$ for ^{156}Dy with a deep potential. However, reducing χ to half the mean field strength returns ^{152}Dy to a spherical distribution which fits the measured $B(E2)$ strength with effective charges $(e_p,e_n)=(1,0)$.

The equilibrium shape was also calculated in ^{144}Ba for inverse temperature $\beta=4$ MeV^{-1}. ^{144}Ba has $E(2_1^+)=199$ keV [23] and deformation $\beta=0.19$ [24]. This nucleus proved to be extremely deformed ($\beta\approx0.45$) in SMMC with the Baranger-Kumar interaction parameters, but with a deformation well not nearly so deep as for the $A\geqslant154$ dysprosiums (Fig. 16). In this case, the potential was only about 2.5 MeV deep. Baranger and Kumar did not calculate this isotope, so direct comparison with them is not possible in this case. Baranger and Kumar also made no claims that their model is valid for nuclei at such extreme deformation [22].

F. Odd *A*

As mentioned previously, the odd nucleon in an odd mass nucleus violates T reversal symmetry and can break the Monte Carlo sign, even with an interaction free from repulsive contributions. Results from ^{153}Dy are shown below in Figs. 17(a)–17(e). In this case, for our simple Hamiltonian

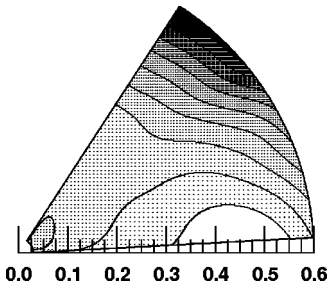

FIG. 16. Shape at $T=0.25$ MeV for ^{144}Ba. 2300 samples. Contour spacing is 0.7 MeV.

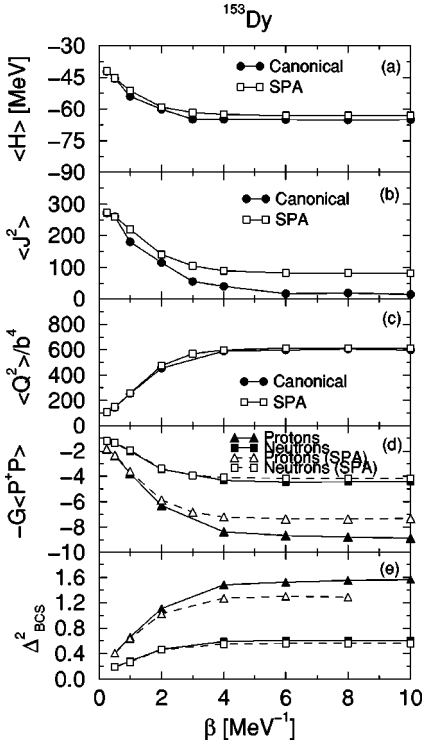

FIG. 17. Energy (a), spin (b), quadrupole moment (c), pairing energy (d), and BCS pair gap (e) in ^{153}Dy for Baranger-Kumar interaction strengths. Symbols for (e) match the symbols in (d).

the Monte Carlo sign behaves well and remains at 0.82 for canonical $\beta=10$. Also, some of this reduction in sign may in fact be due to limits of numerical accuracy in the machine.

1. Static observables

Results for static observables are quantitatively similar to the even-even results. The energy difference between the full canonical and SPA calculations at $T=100$ keV is 1.97 ± 0.4 MeV [Fig. 17(a)], which is a little less than the 2.49 ± 0.16 MeV canonical-SPA energy difference in neighboring ^{152}Dy and the 2.15 ± 0.06 difference in ^{154}Dy. This difference is due to different pairing energies in these odd-even and even-even isotopes. The discrepancy in $\langle J^2\rangle$ between SPA and full solutions is $\Delta J^2=66$ or $\Delta J\approx8$ [Fig. 17(b)]. The ground state spin for ^{153}Dy is $(7/2)^-$ so that $\langle J^2\rangle=15.75$ and the first excited state is $(3/2)^-$ at excitation $E=109$ keV. Thus, the estimated β needed for filtering the ground state is reachable and $\langle J^2\rangle=16\pm4$ in the SMMC canonical ensemble agrees very well with experiment. Again, the SPA quadrupole moment in ^{153}Dy is in excellent agreement with the full canonical calculation [Fig. 17(c)]. The total pairing energy and BCS gaps [Figs. 17(d) and 17(e)] are similar to results in ^{152}Dy and ^{154}Dy [Figs. 3(a)–3(e)].

Occupation numbers for protons and neutrons in the canonical ensemble for ^{153}Dy appear in Figs. 18(a) and 18(b). As the temperature increases to $T=2$ MeV, the proton occupation shifts only slightly to the highest orbitals. For neutrons, however, there is a clear rise in the $i_{13/2}$ occupation. The occupation numbers are also compared for full canonical

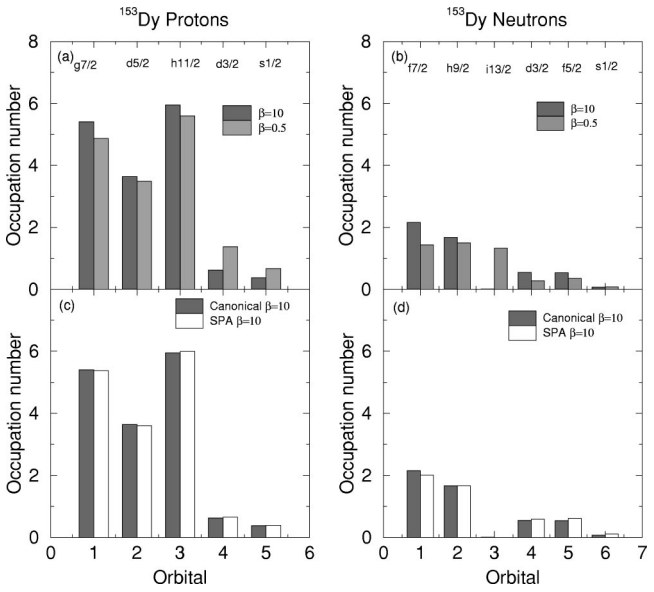

FIG. 18. Proton and neutron occupations in ^{153}Dy. Results (a) and (b) are for the canonical ensemble at $T=0.1$ MeV and $T=2$ MeV while (c) and (d) are canonical vs SPA at $T=0.1$ MeV.

vs SPA calculations in ^{153}Dy for $\beta=10$ in Figs. 18(c) and 18(d). These occupation numbers look very similar, though the agreement is slightly better for the protons. Pairing strengths are more revealing.

The pairing strengths in both proton and neutron channels has also been computed [Figs. 19(a) and 19(b)]. The sum of these eigenvalues, with no background subtraction, in $p\,(n)$ $J=0^+$ channels is 2.30 (0.39) for the exact canonical solution and 1.70 (0.27) in the SPA. These values are stronger in the full canonical than in the SPA, as would be expected from looking at Fig. 17(b). For the protons, the difference in the eigenvalue sum is mostly due to eigenvalue number 2, where the full canonical eigenvalue is more than twice the SPA result. These eigenvalues are otherwise distributed very similarly in the full and SPA results. A similar situation holds for the neutrons, where the first eigenvalue for the full canonical solution is more than double the SPA value. The SPA in the density decomposition does not produce the nuclear pair condensate revealed in the exact calculation.

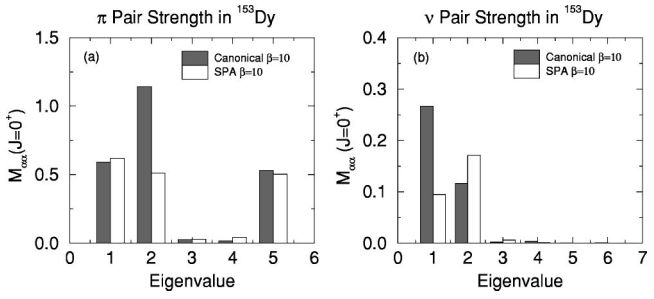

FIG. 19. (a) Pairing matrix eigenvalues for protons in $J^\pi=0^+$ for ^{153}Dy at $T=0.1$ MeV. (b) Pairing matrix eigenvalues for neutrons in $J^\pi=0^+$ for ^{153}Dy at $T=0.1$ MeV.

2. Cranking

With cranking at $\beta=10$ MeV^{-1}, the sign for ^{153}Dy is 0.69 for $\omega=0.05$ MeV, 0.52 for $\omega=0.1$ MeV, and just 0.10 for $\omega=0.2$ MeV. Recall that the sign for $\beta=10$ MeV^{-1} in uncranked ^{153}Dy is 0.82. The moment of inertia $\mathcal{I}_2$ is 49.6 ± 3 $\hbar^2$/MeV in the limit $\omega\to0$ for the canonical calculation.

G. Level density

The level density results for ^{154}Dy are shown in Figs. 20 and 21. $E(\beta)$ points are calculated at intervals of $\Delta\beta=0.0625$ to execute the saddle point inversion to the level density $\rho(E)$ [Eq. (18)]. The level density [Fig. 20(a)] is compared with a few parametrizations of backshifted Fermi gas formulas. The ^{154}Dy density is not directly compared with experimental data since no measurements are available. SMMC results are not as accurate for low temperatures or small excitation energies ($E<1$ MeV) since numerical errors tend to be larger there. This is not a serious concern since the saddle point approximation itself is not really valid at the lowest energies anyway. For the lowest energies, the density of states is best determined by simple state counting from known experimental levels.

Three versions of Fermi gas density formulas are used. The first, labeled BBF with $a=19.25$ and $\delta=1.0$ in Fig. 20(a), is the classic Bethe formula [17]:

$$\rho(E)=\frac{1}{12a^{1/4}(E-\delta)^{5/4}}\exp[2\sqrt{a(E-\delta)}]. \qquad (20)$$

The calculation for ^{154}Dy was done with $a=A/8=19.25$ MeV^{-1} and the energy is backshifted as $E-\delta$ for $\delta=1$ MeV for an even-even nucleus. This formula happens to agree quite well with the SMMC prediction for the ^{154}Dy density for energies above 2 MeV. Notice that solutions to this formula will diverge as $E\to\delta$ for positive δ, so the result is shown only down to an energy where the density formula yields a sensible result.

Holmes, Woosley, Fowler, and Zimmerman (HWFZ) calculate backshifted level densities as [18]

$$\rho(E)=\frac{0.482}{A^{5/6}}(E-\delta)^{-3/2}\exp[2\sqrt{a(E-\delta)}]. \qquad (21)$$

The a parameters for HWFZ can depend on whether the nucleus is deformed or not. For ^{154}Dy, $\delta=0.89$ MeV and $a=22.28$ MeV^{-1} for spherical parameters and $a=20.05$ for the deformed parametrization. The spherical HWFZ curve is always slightly low and the magnitude tails off too quickly below $E=2.5$ MeV as compared with the SMMC result. HWFZ (spherical) is too small by a factor 2.5 at $E=10$ MeV and too low by a factor of 4 at $E=1.5$ MeV. HWFZ (deformed), which has a smaller a parameter, is clearly a worse fit. It is more than an order of magnitude smaller at $E=10$ MeV and is six times smaller at $E=1.5$ MeV. The typical BBF a parameter, $A/8$, is

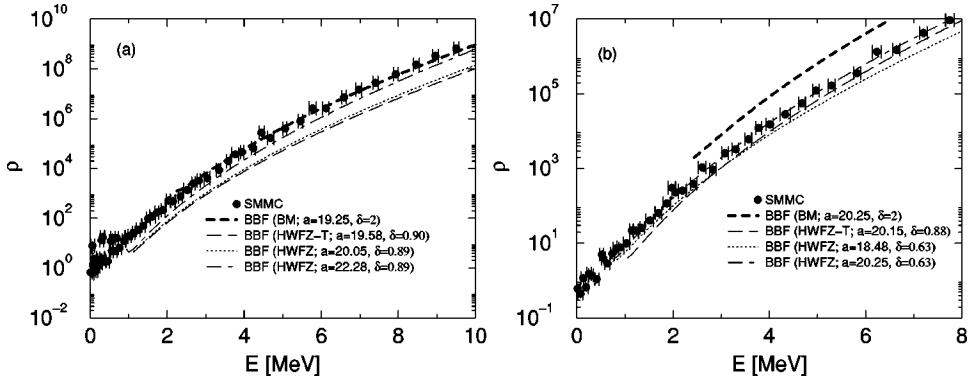

FIG. 20. (a) Level density for ^{154}Dy in SMMC shown with backshifted Fermi gas approximations. BBF=standard backshifted Bethe formula. HFWZ=parametrization of Holmes, Woosley, Fowler, and Zimmerman, and HWFZ-T=HWFZ formula with Cowan-Thielemann-Truran parameters. See text. HWFZ with $a=22.28$ is for spherical ^{154}Dy parameters while $a=20.05$ is for deformed ^{154}Dy parameters. SPA denotes the SPA result for the level density from SMMC. (b) SMMC result for ^{162}Dy compared with the same backshifted Bethe formula approximations.

19.25 MeV^{-1} for $A=154$. This is smaller than the HWFZ (deformed) density parameter and would make the fit even worse.

Cowan, Thielemann, and Truran [20] have modeled the parameters δ and a slightly differently from HWFZ. In this paper, these are called HWFZ-T parameters. He has taken δ as

$$\delta=\Delta(Z,N)-10/A \tag{22}$$

with

$$\Delta(Z,N)=\begin{cases} 12/\sqrt{A}, & \text{even-even} \quad (23)\\ -12/\sqrt{A}, & \text{odd-odd} \quad (24)\\ 0, & \text{odd.} \quad (25)\end{cases}$$

He obtained the density parameter a from a fit to experimental densities at one neutron separation energy [19,20]. For ^{154}Dy, this gives $\delta=0.90$ and $a=19.58$. The HWFZ-T level density is somewhat lower than the calculated SMMC density in ^{154}Dy at all energies, but the slope agrees pretty well with the SMMC calculation. The HWFZ-T magnitude is lower by a factor 15 at $E=10$ MeV for ^{154}Dy and a factor 6 for $E\approx 1.5$ MeV.

Certainly for the case of ^{154}Dy, the most naive Bohr-Mottelson Fermi gas formula works much better than the more carefully developed parametrizations of HWFZ and Cowan *et al.* This serves as an example of the utility of more realistic SMMC calculations to determine nuclear level densities.

From the specific heat (Fig. 21) and the known E vs β, the ^{154}Dy density calculation is expected to be valid up to 10–15 MeV excitation before finite model space effects set in. The specific heat will increase with increasing temperature. Eventually, however, the model space will become exhausted as the valence particles are all promoted as high in energy as possible within the finite space. The turnover point where C_v stops decreasing is taken as the limit of validity for the calculation. An inert core is assumed here at all times.

The SPA level density for ^{154}Dy has also been calculated and compared with SMMC (Fig. 22). Here, the excitation energy has been taken relative to the SPA ground state. The SPA level density agrees well with SMMC for low excitation energies, but is consistently lower for energies above 4 MeV. Recall that the SPA energy E vs β [Fig. 1(d)] agrees with the full SMMC at high temperatures, but never cools completely to the SMMC value for lower temperatures. Thus ΔE from $T=0$ to $T=\infty$ is smaller in the SPA than in the full canonical SMMC, and this difference of a couple of MeV makes a perceptible difference in the level density. At $E=10$ MeV, the SPA density is smaller by a factor of 4.

It is in a sense peculiar that although the SPA energy agrees well with the SMMC energy at high temperatures, the level density just mentioned above agrees worse at high temperatures than at low. Whether the SPA level density appears better or worse for low or high temperatures depends on what ground state reference is used. A shifted plot with the

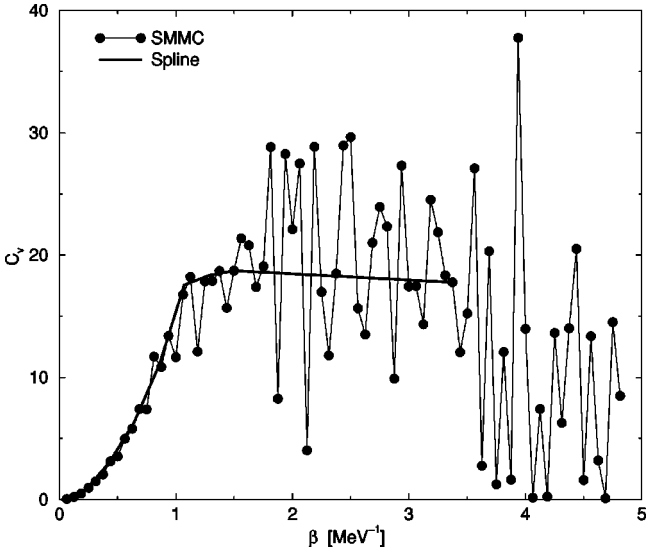

FIG. 21. Heat capacity in ^{154}Dy.

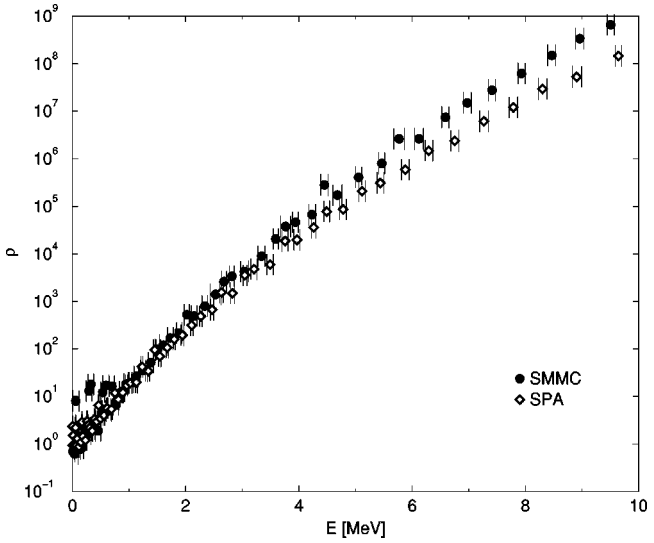

FIG. 22. SPA vs SMMC level density in ^{154}Dy.

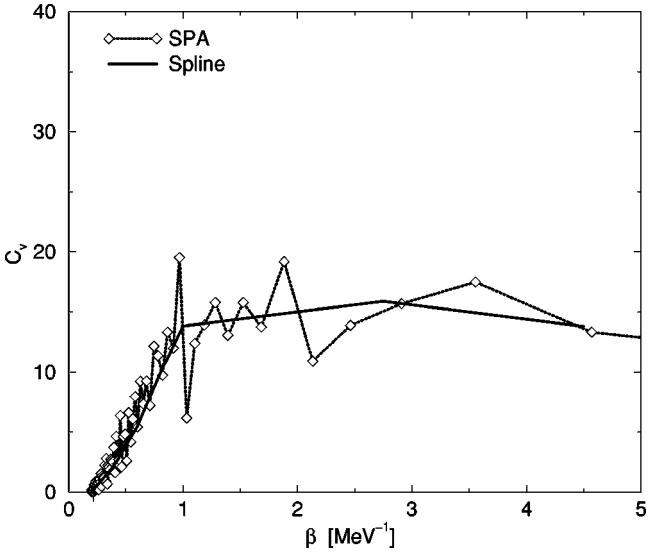

FIG. 24. SPA heat capacity in ^{154}Dy.

SPA energy referred to the SMMC ground state instead leads to better agreement at high temperatures and worse at low temperatures (Fig. 23).

The heat capacity can be found in Fig. 24. This looks similar to the full SMMC calculation except that the magnitude of C_v is smaller except for the lowest temperatures (highest β). The heat capacity has a sharp dropoff below $E=1$ MeV for both SPA and full SMMC solutions. The heat curve implies that the SPA should be valid for up to about 13 MeV excitation. However, the SPA density clearly diverges from SMMC well before this limit.

Similar calculations are shown for ^{162}Dy in Fig. 20(b). For the more deformed ^{162}Dy, the HWFZ-T formula works comparatively well as Fermi gas estimates go, but is still off by a factor 3 near $E=1$ MeV and a factor 1.4 near $E=10$ MeV. HWFZ in ^{162}Dy is better than HWFZ-T at low energies, but is clearly worse at higher energies. It is within a factor 2 of SMMC for $E=1$ MeV and smaller than SMMC by a factor of 3 at $E=10$ MeV. In contrast to ^{154}Dy, HWFZ fits very well for ^{162}Dy using $a=A/8=20.25$ MeV^{-1}. The simple backshifted Bethe formula fails badly here, however, especially for higher energies.

We determined that the level density calculation for this isotope is valid up to excitations of 15–20 MeV. This is slightly higher than the valid range for the density in ^{154}Dy.

The comparison of SMMC density in ^{162}Dy with the Tveter *et al.* [21] data is displayed in Fig. 25. The experimental method of Tveter *et al.* can reveal fine structure, but does not determine the absolute density magnitude. The SMMC calculation is scaled to facilitate comparison. In this case, the scale factor has been chosen to make the curves agree at lower excitation energies. From 1 to 3 MeV, the agreement is very good. From 3 to 5 MeV, the SMMC density increases more rapidly than the data. This deviation from the data cannot be accounted for by statistical errors in either

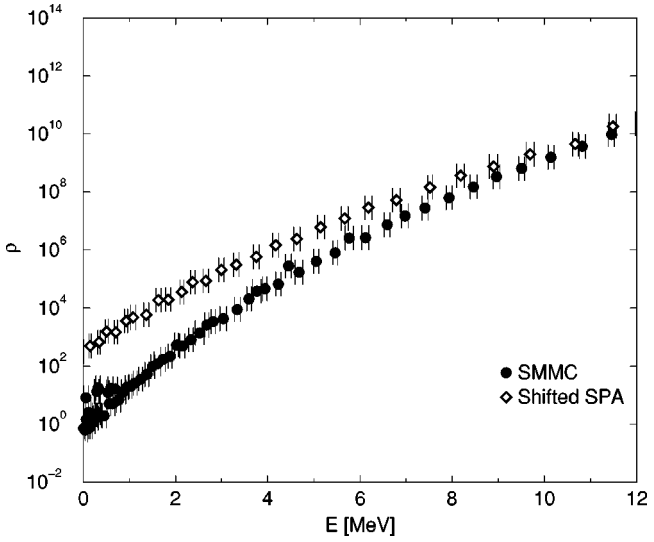

FIG. 23. SPA level density with energy shift in ^{154}Dy. See text for explanation.

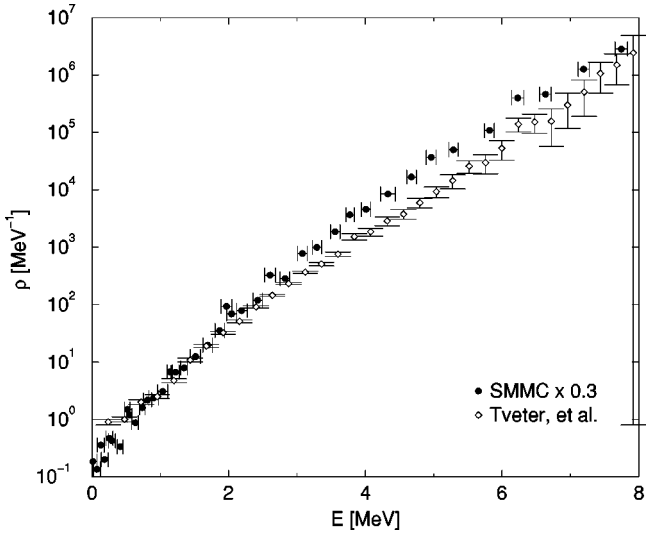

FIG. 25. SMMC density vs data in ^{162}Dy.

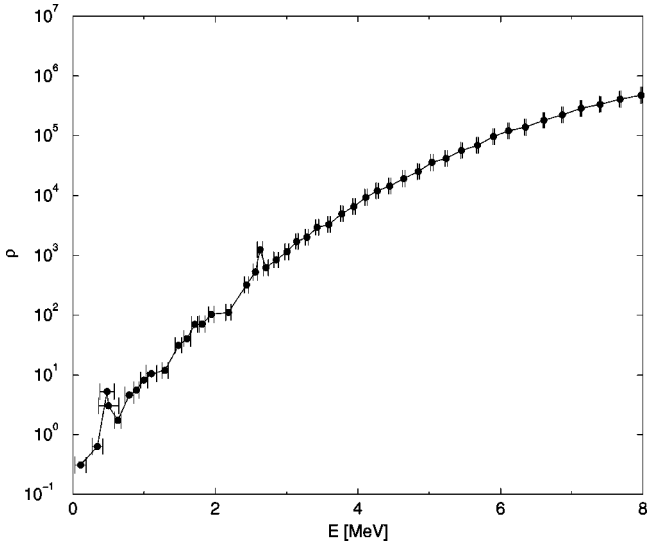

FIG. 26. SMMC density in ^{140}Ba.

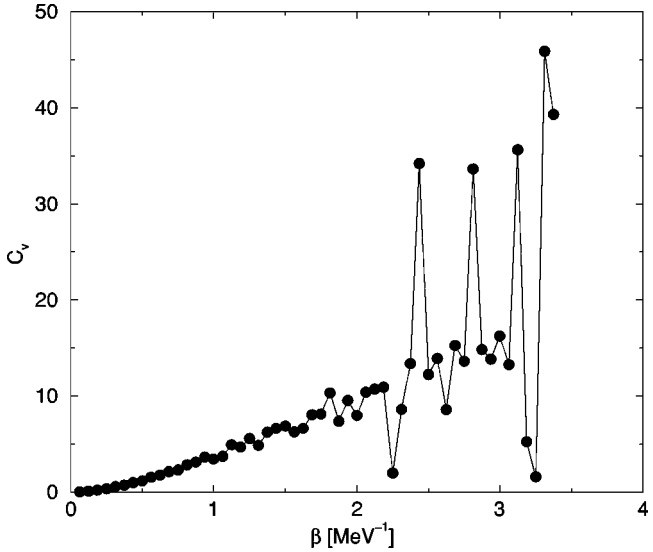

FIG. 27. SMMC heat capacity in ^{140}Ba.

the calculation or measurement. Near 6 MeV, the measured density briefly flattens before increasing and this also appears in the calculation, but the measurement errors are larger at that point.

The measured density includes all states included in the theoretical calculation plus some others, so that one would expect the measured density to be greater than or equal to the calculated density, and never smaller. We could have chosen our constant instead to match the densities for moderate excitations and let the measured density be higher than the SMMC density for lower energies (1–3 MeV).

Comparing structure between SMMC and data is difficult for the lowest energies due to statistical errors in the calculation, and comparison at the upper range of the SMMC calculation, i.e., $E \approx 15$ MeV, is unfortunately impossible since the data only extend to about 8 MeV excitation energy.

Level density information has also been calculated for the lighter nearer closed shell nucleus ^{140}Ba. This was done to investigate possible systematic differences in level densities. Its level density is shown in Fig. 26 and the specific heat in Fig. 27. Unlike the dysprosiums, the calculated heat capacity curve in ^{140}Ba is very flat.

H. Changing the model space

Whether or not one has included enough configurations in the model space is always an issue in these types of calculations. As mentioned in Sec. II F, we examined deformations and moments of inertia in an enlarged model space including the unique-parity orbit below our original space, i.e., $g_{9/2}$ for protons and $h_{11/2}$ for neutrons. The deformations of ^{152}Dy and ^{156}Dy remained unchanged. The moments of inertia for ^{156}Dy differ by only a few percent in the new model space and this difference was within the sampling errors of the calculation. Thus, enlarging the model space in this way does not seem to make any difference in the results. We further attempted calculations for the entire two-shell space used by Baranger and Kumar, but were unable to go to β values higher than about 1 due to the prohibitive amount of computer time required.

IV. SUMMARY

The work has systematically laid the groundwork for applying the shell model in rare earths. Previous applications have been plagued by severely truncated model spaces. An advantage of being able to explore exact shell model solutions in more expansive model spaces is to explain in fundamental ways behaviors such as band crossings and pair correlations that have been previously understood from phenomenological models.

The static path approximation done in density decomposition for this phenomenological pairing plus quadrupole model works well for calculating deformation and relative energy differences between ground states of different isotopes regardless of deformation. Additionally, deformations are well determined in the SPA for quadrupole coupling strengths even a factor of 3 larger than the Baranger-Kumar mean field values.

The density decomposition SPA results for the pairing energy and pair gaps are not as good, however, and the discrepancy is worse for increasing pair strengths. The SPA also overestimates the low-spin moments of inertia. However, the SPA does produce the $\nu i_{13/2}$ band crossing at the predicted spin for ^{156}Dy. The SPA does not produce the ground state nuclear pair condensate and pair gap; hence the discrepancies in energy and moments of inertia.

SPA in the ''natural'' decomposition might lead to better moment of inertia results. Additionally, we note that Rossignoli, Ansari, and Ring have applied spin projection in the SPA to improve agreement for $\langle J^2 \rangle$ at low T in deformed systems [25].

The low-spin SMMC moment of inertia in ^{156}Dy for this Hamiltonian agrees well with experiment. As expected, the calculated moment of inertia initially increases and then decreases. The decreasing moment of inertia in ^{156}Dy is ac-

companied by rising $J=12$ pair strength, which is interpreted as a signal for the $i_{13/2}$ band crossing. This is seen in both the SMMC and SPA results.

Deformations in the canonical ensemble with Baranger-Kumar parameters agree with both Baranger-Kumar and experimental results for isotopes tested that appear in their paper [6], but deformations calculated for some other nuclei do not. Also, the deformation wells in dysprosiums with $A \geqslant 156$ are very deep at low temperatures, i.e., below $T \sim 0.25$ MeV. The lightest isotope studied, ^{152}Dy, is clearly too deformed in its ground state. The calculated $B(E2)$ strengths require a reduced fitted effective charge for $A \leqslant 154$, confirming that the light dysprosiums are excessively deformed in their ground states for this Hamiltonian.

ACKNOWLEDGMENTS

J.W. is very grateful to T. L. Khoo, K. Langanke, W. Nazarewicz, and P. Vogel for useful discussions. This work was supported in part by the National Science Foundation, Grant Nos. PHY-9722428, PHY-9420470, and PHY-9412818. This work was also supported in part through Grant No. DE-FG02-96ER40963 from the U.S. Department of Energy. Oak Ridge National Laboratory (ORNL) is managed by Lockheed Martin Energy Research Corp. for the U.S. Department of Energy under Contract No. DE-AC05-96OR22464. We also acknowledge use of the CACR parallel computer system operated by Caltech and use of MHPCC SP2 systems.

[1] R. Rossignoli, Phys. Rev. C **54**, 1230 (1996).
[2] R. Rossignoli, N. Canosa, and J. L. Egido, Nucl. Phys. **A605**, 1 (1996).
[3] D. J. Dean, S. E. Koonin, G. H. Lang, P. B. Radha, and W. E. Ormand, Phys. Lett. B **317**, 275 (1993).
[4] E. Caurier, G. Martinez-Pinado, F. Nowacki, A. Poves, J. Retamosa, and A. P. Zuker, preprint nucl-th/9809068.
[5] D. J. Dean, S. E. Koonin, and K. Langanke, Phys. Rep. **278**, 2 (1997).
[6] M. Baranger and K. Kumar, Nucl. Phys. **A110**, 529 (1968).
[7] T. L. Khoo (private communication).
[8] W. E. Ormand, D. J. Dean, C. W. Johnson, G. H. Lang, and S. E. Koonin, Phys. Rev. C **49**, 1422 (1994).
[9] H. Nakada and Y. Alhassid, Phys. Rev. Lett. **79**, 2939 (1997).
[10] Y. Alhassid and B. Bush, Nucl. Phys. **A549**, 43 (1992).
[11] K. Langanke, D. J. Dean, S. E. Koonin, and P. B. Radha, Nucl. Phys. **A613**, 253 (1997).
[12] L. S. Kisslinger and R. A. Sorensen, Rev. Mod. Phys. **35**, 853 (1963).
[13] H. W. Cranmer-Gordon, P. D. Forsyth, D. V. Elenkov, D. Howe, and J. F. Fisher-Schafer, Nucl. Phys. **A465**, 506 (1987).
[14] W. C. Ma *et al.*, Phys. Rev. Lett. **61**, 46 (1988).
[15] W. D. Myers and W. J. Swiatecki, Nucl. Phys. **81**, 1 (1966).
[16] Y. Alhassid, G. F. Bertsch, D. J. Dean, and S. E. Koonin, Phys. Rev. Lett. **77**, 1444 (1996).
[17] H. A. Bethe, Rev. Mod. Phys. **9**, 69 (1937).
[18] J. A. Holmes, S. E. Woosley, W. A. Fowler, and B. A. Zimmerman, At. Data Nucl. Data Tables **18**, 305 (1976).
[19] G. Rohr, Z. Phys. A **318**, 299 (1984).
[20] J. J. Cowan, F. K. Thielemann, and J. W. Truran, Phys. Rep. **208**, 267 (1991).
[21] T. Tveter, L. Bergholt, M. Guttormsen, E. Melby, and J. Rekstad, Phys. Rev. Lett. **77**, 2404 (1996).
[22] M. Baranger and K. Kumar, Nucl. Phys. **A110**, 490 (1968).
[23] *Table of Isotopes*, 8th ed., edited by Richard B. Firestone and Virginia S. Shirley (Wiley, New York, 1996).
[24] S. Raman, C. H. Malarkey, W. T. Milner, C. W. Nestor, Jr., and P. H. Stelson, At. Data Nucl. Data Tables **36**, 7 (1987).
[25] R. Rossignoli, A. Ansari, and P. Ring, Phys. Rev. Lett. **70**, 1061 (1993).